ACS OMEGA

Open Access



http://pubs.acs.org/journal/acsodf

Article

# γ-Ray-Induced Photocatalytic Activity of Bi-Doped PbS toward Organic Dye Removal under Sunlight

Jeya P, Keerthana SP, L. Kungumadevi,* Yuvakkumar Rathinam,* Ravi Ganesan, Asokan Kandasami, and T. S. Senthil

Cite This: *ACS Omega* 2023, 8, 47427−47439

Read Online

ACCESS | Metrics & More | Article Recommendations

**ABSTRACT:** Photocatalysts based on semiconducting chalcogenides due to their adaptable physio-chemical characteristics are attracting attention. In this work, Bi-doped PbS (henceforth PbS:Bi) was prepared using a straightforward chemical precipitation approach, and the influence of γ-irradiation on PbS's photocatalytic ability was investigated. Synthesized samples were confirmed structurally and chemically. $Pb_{(1-x)}Bi_xS$ ($x$ = 0, 0.005, 0.01, 0.02) samples that were exposed to gamma rays showed fine-tuning of the optical bandgap for better photocatalytic action beneath visible light. The photocatalytic degradation rate of the irradiated $Pb_{0.995}Bi_{0.005}S$ sample was found to be 1.16 times above that of pure PbS. This is due to the occupancy of $Bi^{3+}$ ions at surface lattice sites as a result of their lower concentration in PbS, which effectively increases interface electron transport and the annealing impact of gamma irradiation. Scavenger tests show that holes are active species responsible for deterioration of the methylene blue. The irradiated PbS:Bi demonstrated high stability after being used repeatedly for photocatalytic degradation.

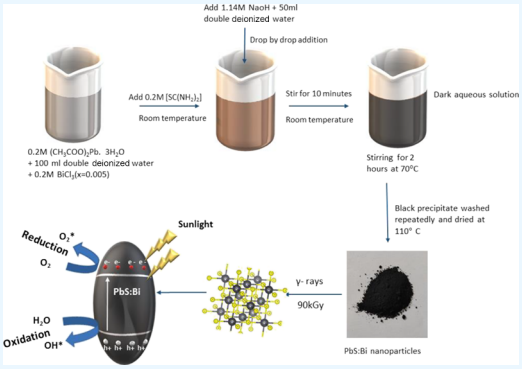


## 1. INTRODUCTION

Nanostructured semiconductors are dominating several sectors because of extremely high surface-to-volume, quantum confinement in the nanoregime, high surface energy, and increased defect states.[1−4] These nanomaterials have commendable advantages because their physical, chemical, and surface morphology can be tuned by changing their shape, size, and application.[5−7] Semiconductor catalysts are efficient, cheap, and simple to synthesize[1,2] in a variety of morphologies. Semiconductor photocatalysts have applications in various fields of catalysis, including photochemistry, electrochemistry, inorganic and organic chemistry, and so on. They also offer promising solutions to environmental pollution problems, and their tunable physical and chemical properties make them a potential photocatalytic element.[8−10] Lead sulfide (PbS) is the most common IV−VI semiconductor chalcogenide on Earth, with a bulk bandgap of 0.41 eV at 300 K.[11] They have strong quantum confinement in the nanoregime due to their large excitonic Bohr radius (18 nm), allowing them to fine-tune their properties for desired applications.[11,12] PbS has an exceptional ability to absorb visible-light radiation.[11] The specific area increases as one moves closer to the nanoscale, increasing the number of active sites and improving photocatalytic efficiency. Furthermore, because they are insoluble in water and settle as precipitate, we can reuse them multiple times without losing much of their degrading efficiency of organic contaminants. Due to these remarkable characteristics, PbS is a promising photocatalyst to degrade contaminants.

To develop semiconducting material's photocatalytic properties, a number of approaches are utilized. Among these are doping, nanocomposites, and high-energy/ion irradiation, which change the shape and particle size of nanomaterials to enhance their photocatalytic activity.[13−21] Doping is an effective method for altering the material's properties.[22] By introducing defect states through doping, the physical and chemical nature of semiconducting materials can be modified to increase material's photoresponsiveness. Consequently, dopant elements are crucial for fine-tuning defect levels in the host material. Physical, electrical, and optical nature of PbS modified by dopant elements such as aluminum, chromium, cadmium, cobalt, manganese, nickel, copper, bismuth, terbium, etc. has been reported.[23−31] Ajibade et al. decomposed the organic pollutant methylene blue (MB) with a PbS photocatalyst with a degradation efficiency of 75.9% after 180 min of ultraviolet irradiation.[32] By adding two dopants (Mg and Zn)

Received: April 25, 2023
Revised: August 29, 2023
Accepted: August 30, 2023
Published: December 8, 2023

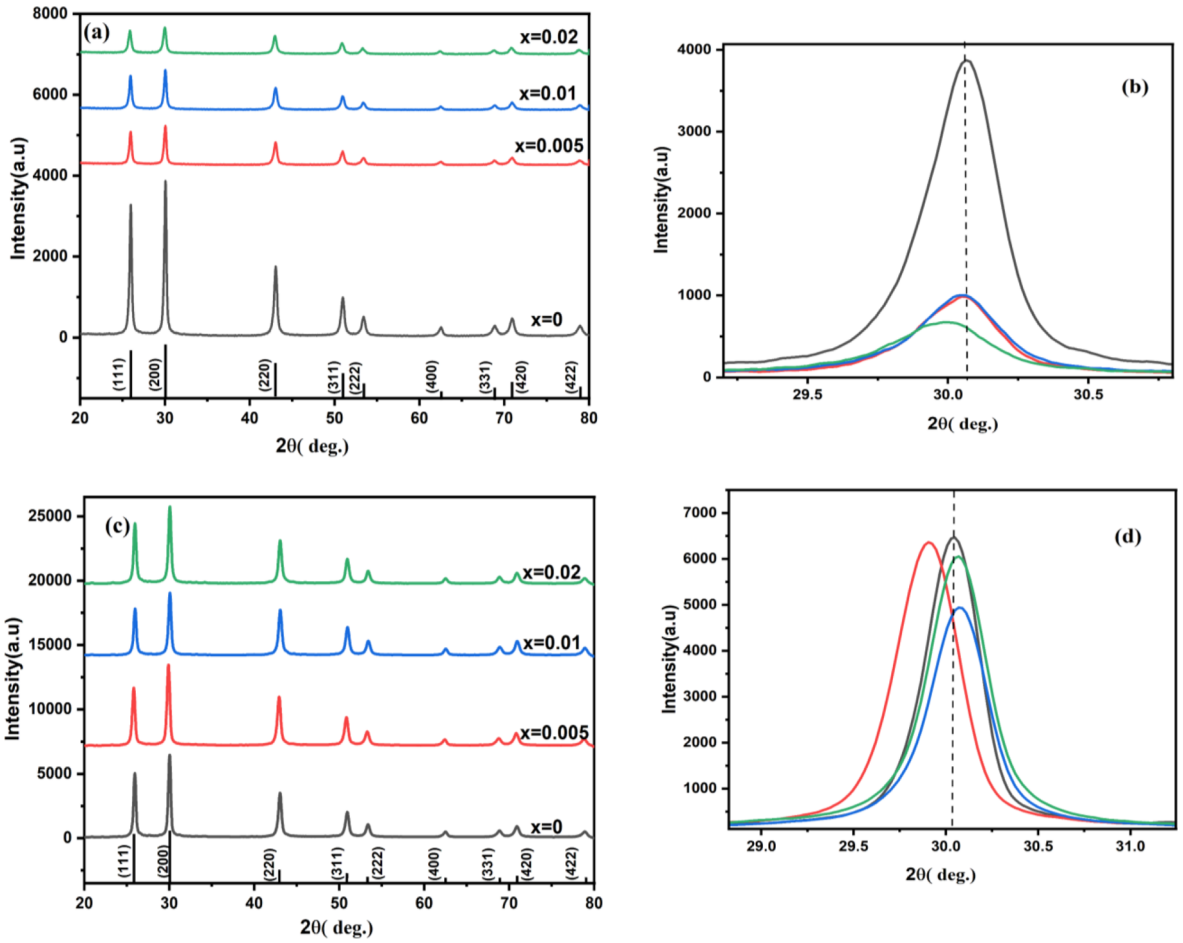


**Figure 1.** XRD pattern of (a) pure PbS:Bi, (b) (200) plane, and (c) $\gamma$-irradiated PbS:Bi (d) (200) plane.

to PbS, Andrade Neto et al.[3] enhanced the photocatalytic performance and destroyed about 80% of MB under comparable conditions. Here, the photocatalytic activity of heterovalent cationic doping of PbS with Bi ions is examined. $Bi^{3+}$ (1.03 Å ionic radius) is comparable to $Pb^{2+}$ (1.19 Å), making it an ideal option for Pb sites. Due to the narrow bandgap of the Bi element, they can be used as an efficient photocatalyst. When $Bi^{3+}$ ions are substituted for $Pb^{2+}$ ions as dopants at Pb sites, the recombination rate is slowed and the lifespan of photoassisted charge carriers is lengthened, guiding to improved photocatalytic activity. Dong et al. prepared Bi by the chemical solution technique and reported stable and remarkable photocatalytic activity of Bi nanoparticles toward NO removal by surface plasmon resonance of the Bi element.[33]

In recent years, high-energy $\gamma$-irradiation's impact on nanomaterials has been the subject of extensive study.[17,34] These high-energy gamma rays can penetrate the crystal lattice and cause changes to the material's physical properties.[34−38] Depending on the energy of the $\gamma$-rays, they interact with matter in one of the three ways: either through Compton scattering, the photoelectric effect, or pair creation. High-energy gamma irradiation causes ionization in the material, which in turn causes defects in the form of an alteration in atoms or ions energy levels that make up the material. They also cause structural alteration, self-assembly, and the annealing effect, as well as the displacement of atoms from their locations in the crystal lattice. Gupta et al.[39] examined the $\gamma$-radiation effect on physical properties of PbSe nanowires, optimizing them for application in optoelectronics. Zhao et al.[40] examined photocatalytic RhB degradation and phenol using gamma-irradiated $TiO_2$.

Several papers and reviews[41−43] have been published on the photocatalytic use of bismuth-based catalysts. A unique technique to examine photocatalytic activity was studied by using high-energy gamma irradiation in PbS:Bi nanocrystallites for efficient degradation of organic MB dye in natural sunlight.

## 2. EXPERIMENTAL SECTION

PbS:Bi nanoparticles were synthesized using a co-precipitation technique. All compounds were of analytical quality, acquired from Sigma-Aldrich, and utilized as it is. Lead acetate trihydrate $[Pb(CH_3COO)_2{\cdot}3H_2O]$ and thiourea $[SC(NH_2)_2]$ were taken in the ratio of 1:1 in 100 mL of double-distilled water and stirred to dissolve. 0.5 M NaOH solution in 50 mL of distilled water is added to the solution very slowly to maintain the pH at 10. Adding NaOH causes the solution to turn a murky brown color; stirring for 10 min transforms it into a black suspension; and stirring this solution for 2 h at 70 °C produces a black solid precipitate in the solution. This dark suspension is let out overnight at room temperature to settle. To get rid of any leftover chemicals or contaminants, the precipitate was centrifuged and cleaned many times with acetone, ethanol, and distilled water. The resulting product is dried at 110 °C for 2 h. The same basic steps described above were used to synthesize the Bi dopant using bismuth trichloride $[BiCl_3]$ in the stoichiometric ratio $Pb_{(1-x)}Bi_xS$,


https://doi.org/10.1021/acsomega.3c02855
ACS Omega 2023, 8, 47427−47439

Table 1. (a) Pure PbS:Bi and (b) γ-Irradiated PbS:Bi

| pristine PbS:Bi | *hkl* | 2θ | lattice parameter (*a*) (Å) | *D* (nm) | δ in $10^{15}$ ($m^{-2}$) | microstrain × $10^{-3}$ | stacking fault (SF) × $10^{-3}$ | average crystallite size (nm) |
|---|---|---|---|---|---|---|---|---|
| | | | | | (a) | | | |
| *x* = 0 | (200) | 30.05 | 5.942 | 24.08 | 1.72 | 5.55 | 1.68 | 19.27 |
| *x* = 0.005 | (200) | 30.03 | 5.946 | 21.35 | 2.19 | 6.26 | 1.68 | 16.99 |
| *x* = 0.01 | (200) | 30.03 | 5.945 | 20.29 | 2.4 | 6.59 | 1.99 | 17.67 |
| *x* = 0.02 | (200) | 29.96 | 5.958 | 16.82 | 3.53 | 7.97 | 2.40 | 17.08 |
| | | | | | (b) | | | |
| *x* = 0 | (200) | 30.03 | 5.945 | 27.86 | 1.28 | 4.80 | 1.45 | 21.01 |
| *x* = 0.005 | (200) | 29.87 | 5.977 | 23.29 | 1.84 | 5.77 | 1.74 | 20.18 |
| *x* = 0.01 | (200) | 30.04 | 5.944 | 26.27 | 1.44 | 5.09 | 1.54 | 20.28 |
| *x* = 0.02 | (200) | 30.03 | 5.945 | 26.02 | 1.47 | 5.14 | 1.55 | 20.62 |

where *x* = 0, 0.005, 0.01, 0.02. We then gathered this black powder and performed initial characterizations.

**2.1. Irradiation.** A $^{60}$Co gamma with 1.25 MeV was used to irradiate PbS:Bi powdered samples at a 2.023 kGy/h dosage in a 1200 Gamma chamber in ambient air and room temperature at Inter-University Accelerator Center in New Delhi. All products were exposed to the same extremely high dose of radiation (90 kGy). This dosage was decided after reviewing the relevant literature.[18,38]

**2.2. Characterization.** Using powder X-ray diffraction with Cu-$K_\alpha$ radiations ($\lambda$ =1.5406) in the 2θ range of 20°−80°, we were able to determine the crystal phase of both unaltered and gamma-irradiated PbS:Bi. Field emission scanning electron microscopy (FESEM) and energy-dispersive X-ray spectroscopy (EDAX) were employed to determine the produced samples' structure and elemental composition. PbS:Bi was examined further for its morphology employing a 200 kV JEM 2010 transmission electron microscope (TEM). Using a UV−vis spectrophotometer (UV-3600, Shimadzu, Japan) and a fluorescence spectrophotometer (Horiba Fluorolog 3 TCSPC) with a steady-state 450 W xenon arc lamp, optical investigations of PbS:Bi samples were conducted. We used a confocal Raman microscope (WITec alpha 300RA) equipped with an Ar ion laser beam of wavelength 532 nm to study the defects in both untreated and irradiated PbS:Bi nanoparticles. Quantachrome instruments autosorb iQ Station1 was used to conduct Brunauer−Emmett−Teller (BET) and Barrett−Joyner−Halenda (BJH) studies on samples to analyze their specific surface area. A thermogravimetric analyzer (PerkinElmer) was used to study the sample's heat stability.

**2.3. Photocatalytic Activity.** Recently, the employment of dyes has received constructive criticism, and alternative molecular models have been developed. However, utilizing dye photobleaching as the verification of beginning kinetics of first photodegradation may still be fair, notably in case of MB.[44] MB discoloration in aqueous media is used to evaluate photocatalytic activity.[45] For preliminary evaluation of photocatalytic systems, MB discoloration is still recognized as the way. Here, photocatalytic action of irradiated Bi ion-doped PbS was examined for MB dye contaminant removal under visible light. For photolysis (without a catalyst), 50 mL (10 ppm) of MB solution was exposed to sunlight for 160 min while samples were collected at regular intervals. For photocatalytic dye degradation, 10 ppm of MB solution was added to 0.05 g of chemically produced PbS catalyst. This solution was first stirred up in the dark for 30 min to attain equilibrium between adsorption and desorption before being exposed to sunlight for 160 min. To monitor the reaction, at regular intervals samples were obtained. Before analysis, the photocatalyst in the sample solution was removed, and sample solution absorbance was evaluated at 500−650 nm wavelength employing UV−vis studies.

Photocatalytic degradation was estimated using equation photodegradation percentage (%) = $\frac{A_0 - A}{A_0} \times 100$, where $A_0$ is the absorbance of the initial concentration and after the time (*t*) of MB solution. The Langmuir−Hinshelwood mechanism for MB is derived from the first-order rate $\ln(A_0/A) = kt$, where *k* is the first-order rate constant.[46] Using radical scavengers, the active species responsible for MB degradation was examined and photocatalyst's reusability was also evaluated.

## 3. RESULTS AND DISCUSSION

PbS:Bi nanoparticle X-ray diffraction is revealed in Figure 1a−d. XRD confirms no traceable contamination in the samples. All of the PbS:Bi XRD peaks at 2θ are assigned to the (111), (200), (220), (311), (222), (400), (331), (420), and (422) planes of PbS with a cubic crystal structure. The pristine PbS lattice parameter was found to be well-matched with the PbS JCPDS card No.: 01-072-4873. $Bi^{3+}$ (ionic radius 0.103 nm) is comparable to $Pb^{2+}$ (0.119 nm), $Bi^{3+}$ replaces $Pb^{2+}$ sites. The unmodified cubic structure of PbS:Bi from XRD data confirms this.

The lattice constant can be calculated from the well-known relation: $\frac{1}{D^2} = \frac{\sqrt{h^2 + k^2 + l^2}}{a^2}$. The average crystallite size was estimated from diffraction employing Debye−Scherrer's, $D = \frac{0.9\lambda}{\beta \cos\theta}$, where λ is the wavelength of X-ray radiation (Cu Kα = 1.5418 Å), and β is the full width at half-maximum.[47] The dislocation density ($\delta_{dis}$) was calculated using the equation: $\delta_{dis} = \frac{1}{D^2}$ and the stacking fault was calculated using the equation: $SF = \left\{ \frac{2\pi^2}{45(3\tan\theta)^{1/2}} \right\} \beta_{hkl}$.[48] The crystallite size (*D*), dislocation density ($\delta_{dis}$), microstrain, and stacking fault (SF) of pristine and γ-irradiated PbS:Bi nanocrystallites of the preferential orientation along the (200) plane were calculated and taken for analysis and are shown in Table 1a,b.

In pristine PbS with Bi dopant insertion, we see decreasing XRD peak intensity with increasing FWHM, as well as peak shifting toward a lower diffraction angle. This is due to the dopant effect, which causes structural deformation in the crystal lattice and decreases the crystallite size.[49] The shift in diffraction peaks toward a lower diffraction angle with increasing dopant concentration (*x* = 0.02) indicates lattice


https://doi.org/10.1021/acsomega.3c02855
ACS Omega 2023, 8, 47427−47439

expansion caused by interstitial substitution of the Bi dopant. The crystallite size for preferential orientation was calculated and decreased with dopant concentration from ∼24 to ∼16 nm. The PbS:Bi mean crystallite size was measured and was slightly smaller than 19 nm (pristine PbS) for Bi of $x$ = 0.005 it is ∼16 and ∼17 nm for Bi of $x$ = 0.01, 0.02. This decrease in the crystallite size was caused primarily by the presence of dopant ions in host sites, which causes strain in the crystal lattice. When Bi ions are used as the dopant in PbS, they either occupy $Pb^{2+}$ vacant sites or occupy $Pb^{2+}$ sites and produce $Pb^{2+}$ interstitial, or in PbS interstitial sites. As a result, internal strain develops and the PbSBi crystal structure remains unstable as $Bi^{3+}$ takes up increasing numbers of $Pb^{2+}$ sites in the host lattice. To relieve strain and stabilize the crystal structure, the crystallite size is reduced. As a result, there is an increase in dislocation density, microstrain, and stacking fault of doped samples, resulting in an increase in defect/trap state number in the crystal lattice.[48] The XRD peak intensity of PbS:Bi samples is found to be enhanced by $\gamma$-irradiation. The strongest peak was observed for irradiated PbS($x$ = 0). For irradiated PbS:Bi samples, we see a peak shift in the direction of lower diffraction angle (compared to pristine PbS). The crystallite size of the irradiated PbS (without dopant) sample for the preferential plane (200) was calculated and increased from 24 (pristine PbS) to 27 nm. Irradiated doped PbS samples exhibit a similar increase in the crystallite size; nevertheless, the mean crystallite size of irradiated PbS samples does not change significantly (as shown in Table 1a,b). We also see a peak shift for irradiated doped samples when compared to irradiated PbS. This is due to the influence of the dopant and high energy irradiation, which displaces Bi ions from their lattice sites and changes the crystal structure. Irradiated PbS:Bi has lower dislocation, microstrain, and stacking fault than pristine PbS, reflecting an increase in crystallite size, and a reduction in crystal lattice defects. Ali et al. examined a similar increase in the crystallite size when they used high-dosage gamma irradiation on PbS grown employing the SILAR technique.[38] All of these results support the improvement in crystallinity caused by gamma irradiation.

FESEM images of PbS:Bi nanoparticles are explored in Figure 2. FESEM analysis of pristine PbS:Bi samples revealed a change in morphology with the addition of the dopant. The surface morphology of pristine PbS shows an irregular shape, which gets agglomerated with the dopant (Figure 2a–d). Furthermore, with $\gamma$-irradiation, the morphology of PbS (without dopant) was improved, showing cubic structure with agglomeration. The morphology of irradiated, doped PbS:Bi samples shows agglomeration with large and small cubic structures because of the annealing effect of gamma irradiation (Figure 2e–h).

Two peaks at EDAX of Pb and S elements were detected for the pure PbS sample, and for dopant samples, we could see a small Bi peak (Figure 3). From the atomic concentration of the element, a lower concentration of Bi in PbS can be observed. This reveals that the obtained product contains only Pb, S, and Bi, with Bi as a dopant in the PbS crystal lattice. No additional impurity was present, indicating sample's purity. EDAX analysis shows that the PbS with a lower concentration of Bi dopant shows more $Bi^{3+}$ content (1.44 times) than the higher dopant concentration of PbS:Bi ($x$ = 0.02). This is due to the inhomogeneous distribution of $Bi^{3+}$ ions in PbS during the preparation process and hence they occupy into the surface and shallow lattice sites.[50]

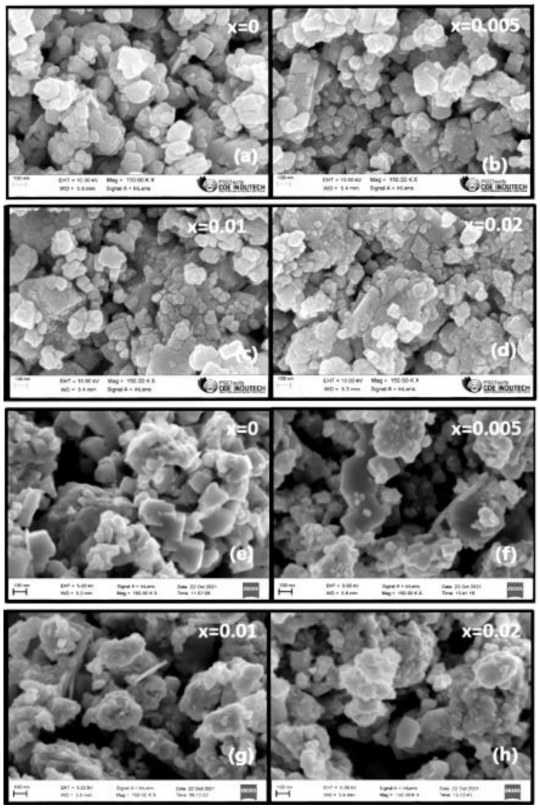


**Figure 2.** FESEM of (a) PbS, (b) PbS:Bi ($x$ = 0.005), (c) PbS:Bi ($x$ = 0.01), (d) PbS:Bi ($x$ = 0.02)) and after gamma irradiation (e) PbS, (f) PbS:Bi ($x$ = 0.005), (g) PbS:Bi ($x$ = 0.01), and (h) PbS:Bi ($x$ = 0.02) in 100 nm scale.

The morphology of the irradiated $Pb_{0.995}Bi_{0.005}S$ sample was reanalyzed with TEM, and it is shown in Figure 4. The HRTEM image confirms the lattice spacing with 0.1702 and 0.139 nm corresponding to (222) and (331) planes which is consistent with the XRD results. The SAED pattern confirms product's crystalline nature.

Raman spectra of pristine and irradiated PbS:Bi were recorded at room temperature and are shown in Figure 5a–d. We observe Raman peaks at 83, 126, 273, 431, 601, and 963 $cm^{-1}$.[51] The peak at 126 $cm^{-1}$ is assigned to TA and LA phonon modes of PbS.[51] The 273 $cm^{-1}$ peaks are assigned to two phonons.[52] The peaks at 431 and 601 $cm^{-1}$ explored first and second overtones of LO phonon, 2LO, and 3LO, respectively.[53] The strong 126 $cm^{-1}$ band and also 273 $cm^{-1}$ broad peak are similar to previously reported data of Cao et al. which are 135 and 274 $cm^{-1}$ excited using 632.8 nm.[51] The peak around 963 $cm^{-1}$ is assigned to $SO_4$ arising from the oxidation of PbS.[51] Though we get the oxidation peak in Raman data, the XRD data confirm PbS purity without any oxidation peaks. 126 $cm^{-1}$ varies with the addition of dopant to PbS without any peak shift. The variation observed in the peak intensity of PbS:Bi is because of gradual incorporation of the Bi dopant in the PbS stoichiometry, which produces stress in the PbS crystal lattice.

With gamma irradiation, the Raman peak intensity of doped samples increased without the appearance of any new vibrational modes. The irradiated doped PbS shows a reduction in the FWHM compared to the pristine doped PbS. The changes observed in the intensity and FWHM of the irradiated $Pb_{0.995}Bi_{0.005}S$ sample denote the reduction in defects


https://doi.org/10.1021/acsomega.3c02855
ACS Omega 2023, 8, 47427−47439

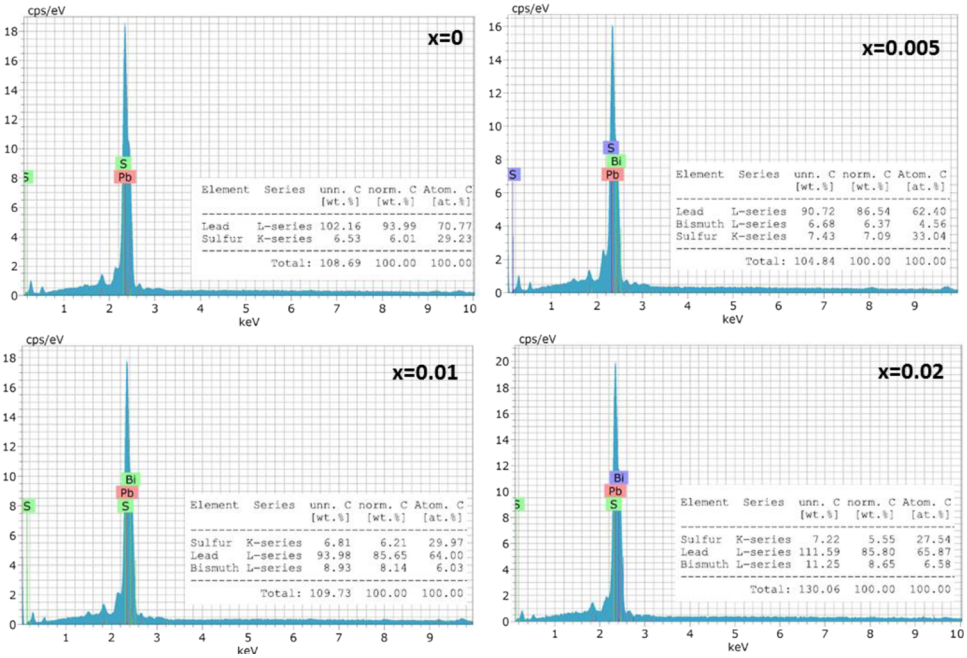


**Figure 3.** EDAX of PbS:Bi ($x$ = 0, 0.005, 0.01, and 0.02).

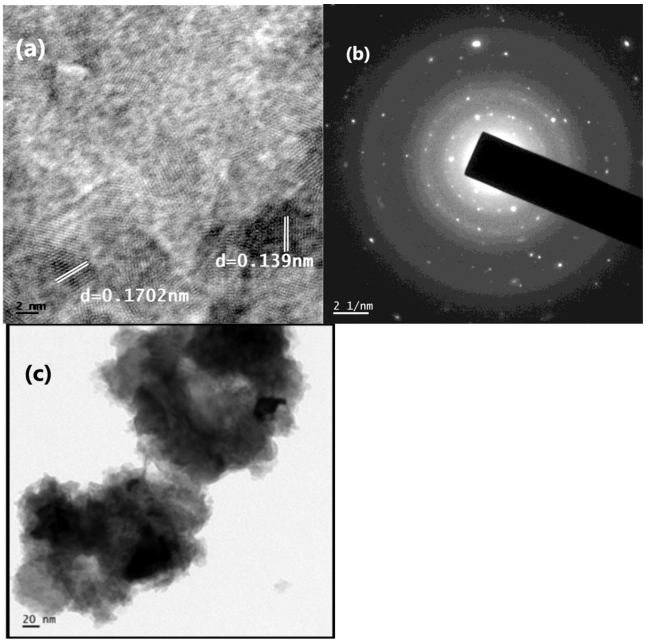


**Figure 4.** HRTEM (a) and SAED (b) and (c) TEM image of $\gamma$-irradiated $Pb_{0.995}Bi_{0.005}S$.

and improvement in the structural properties of PbS:Bi because of annealing of high-energy gamma irradiation.[34]

PbS:Bi optical absorbance was examined employing diffuse reflectance spectroscopy in the range of 200−800 nm. Using data from diffuse reflectance spectra, bandgap ($E_g$) was calculated approximately by employing Kubelka−Munk theory $F(R) = \frac{(1-R)^2}{2R}$, where $R$ is the reflectance.[54] The bandgap and the absorption coefficient ($\alpha$) are related by the Tauc relation as $(\alpha h\nu)^{1/n} = A(h\nu - E_g)$, where $n$ is the power factor of the transition mode (for PbS, $n = 1/2$).[55] The $(\alpha h\nu)^{1/n}$ vs $h\nu$ graph of PbS:Bi is shown in Figure 6a,b. The band gap was obtained from extrapolation of the linear portion of graph toward the $x$-axis as shown in Figure 6.

Bulk PbS has an optical absorption edge in the IR with a bandgap energy of 0.41 eV. However, with the reduction of its crystallite size at the nanoscale, we observe a blue shift in absorption band edge toward the visible region, which is because of the quantum confinement effects of PbS:Bi.[12] The bandgap of pristine PbS is 2.45 eV which slightly increases to 2.6 eV with the influence of dopant concentration. This is due to the defect or trap states created by the dopant element in PbS. However, the band gap has decreased (2.2 eV for pristine) after irradiation and indicates an absorption edge shift (Figure 6). Band gap reduction is because of displacement of atoms from their sites due to the annealing effect of $\gamma$-irradiation.[38] Similar reductions in optical bandgap energy have been reported by Sarker et al. as a result of high-dose gamma irradiation's ability to reduce defects and disorderliness at grain boundaries.[56]

PbS:Bi product photoluminescence studies were performed at room temperature with 337 nm in the spectral range of 300−600 nm (Figure 7). Several emission peaks for all PbS:Bi samples are observed; hence, peak deconvolution was revealed with Gaussian curve fitting. Pristine PbS has the main peak at 429 nm which with the addition of dopants, shifts are explored in Figure 7a−d.

The allowed $^3P_1 \rightarrow {}^1S_0$ transition of the $Bi^{3+}$ ion has been attributed to a broad blue emission band with its center at 446 nm (2.78 eV). Because of the quenching effect, which reduces electron−hole recombination, we notice a drop in peak intensity in doped PbS samples.[38] This is the result of the postdoping disturbance of the density state at the VB edge.[57] After irradiation, PL peak intensity was observed to decrease and it is minimum for PbS:Bi with $x$ = 0.005 sample (Figure 7f). This decrease in peak intensity is due to the annealing effect of $\gamma$-rays, which create sulfur vacancies and also reduce defect states created by dopant ions. Hence, there is recombination rate reduction of electron−hole pairs, which is evident from photoluminescence emission spectra, and this


https://doi.org/10.1021/acsomega.3c02855
ACS Omega 2023, 8, 47427−47439

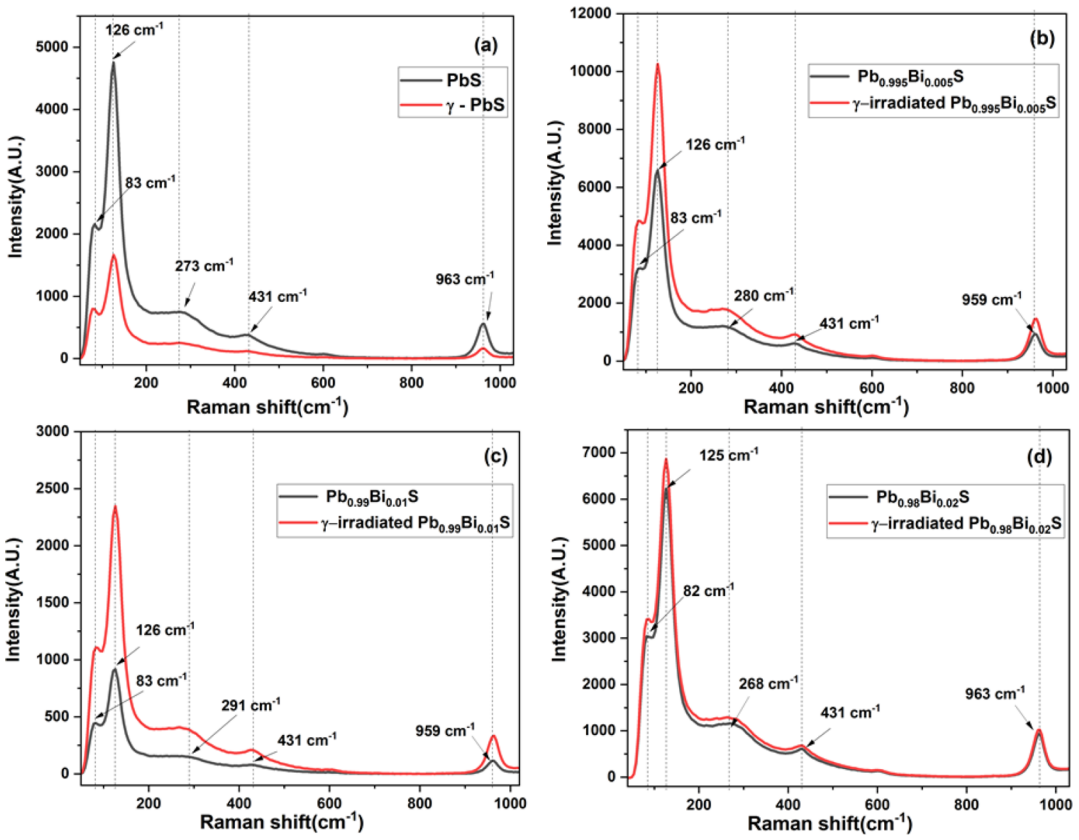


**Figure 5.** Raman spectra of pure and $\gamma$-irradiated (a) PbS, (b) PbS:Bi ($x$ = 0.005), (c) PbS:Bi ($x$ = 0.01), and (d) PbS:Bi ($x$ = 0.02).

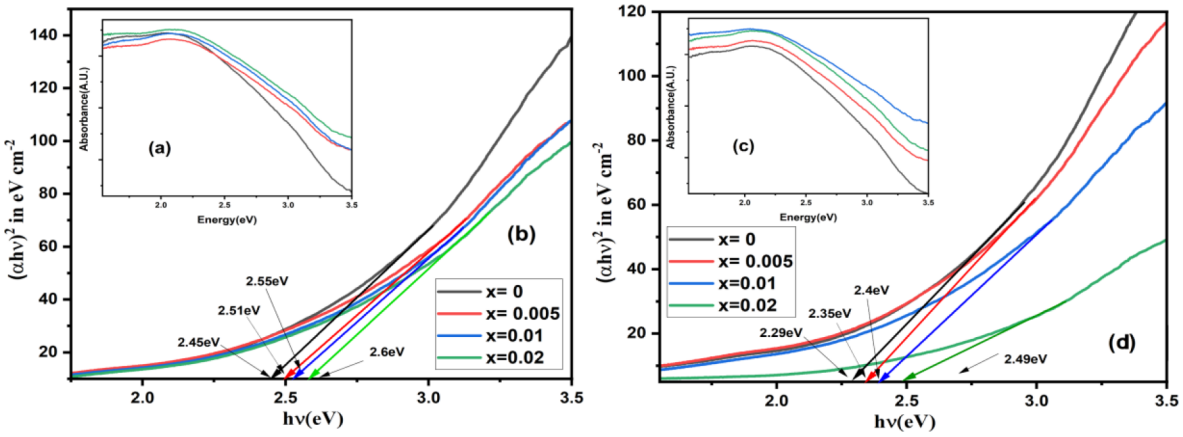


**Figure 6.** (a) Absorbance spectra vs energy (eV) and (b) $(\alpha h\nu)^{1/n}$ vs $h\nu$ (eV) of pure PbS:Bi, and (c) absorbance spectra vs energy (eV) and (d) $(\alpha h\nu)^{1/n}$ vs $h\nu$ (eV) of $\gamma$-irradiated PbS:Bi.

helps to develop photocatalytic action of PbS:Bi.[18,58] The CB and VB potentials are estimated following Mulliken electronegativity theory:[59]

$$E_{VB} = \chi - E^e + 0.5E_g$$

and

$$E_{CB} = E_{VB} - E_g$$

where $E_{VB}$ and $E_{CB}$ are VB and CB edge potentials, respectively. Using electronegativity ($\chi$) and energy of free electrons ($E^e$) on hydrogen scale which is −4.5 eV, the VB potential $E_{VB}$ was 0.80 and 0.83 eV for PbS and PbS:Bi with 0.005% of Bi, respectively. For the same after $\gamma$-irradiation, it was calculated to be 0.725 and 0.755 eV. The calculated $E_{CB}$ for pristine PbS and PbS:Bi with 0.005% of Bi was −1.64 and −1.67 eV, whereas for after $\gamma$-irradiation, it was −1.56 and −1.59 eV. The difference in electronegativity between $Bi^{3+}$ and the host $Pb^{2+}$ raises conduction and lowers the valence band during doping. Nevertheless, after irradiation, the conduction band is lowered and the valence band is raised. This is because of the displacement of atoms which creates sulfur vacancies and also forms shallow levels in the forbidden gap and this shows modified electron−hole pair recombination.

Thermogravimetric and differential thermal analysis was performed to study thermal stability in nitrogen flow over a temperature range of 900 °C for irradiated $Pb_{0.995}Bi_{0.005}S$



https://doi.org/10.1021/acsomega.3c02855
ACS Omega 2023, 8, 47427−47439

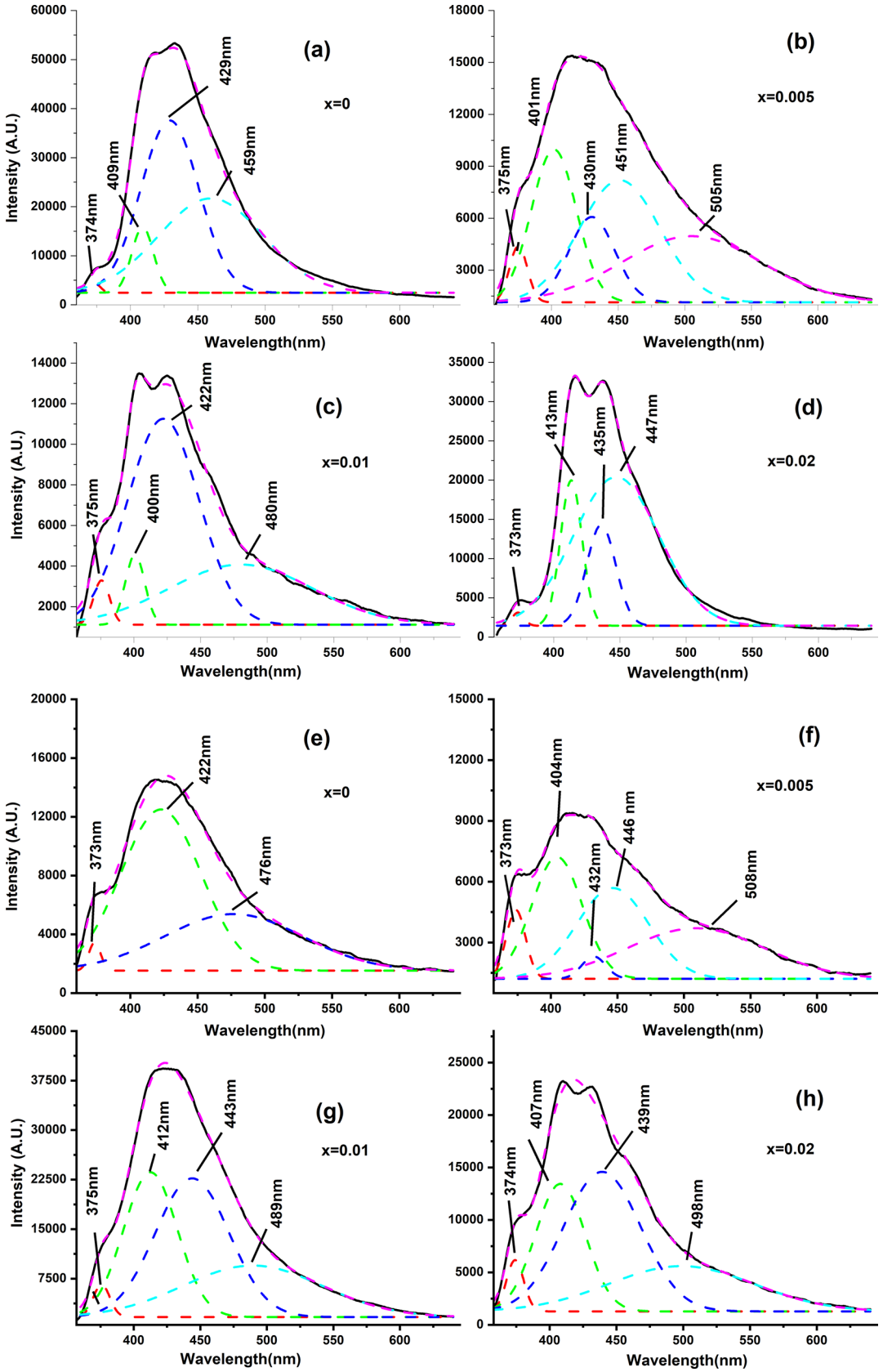


**Figure 7.** Photoluminescence spectra of pristine PbS:Bi of $x = 0$ (a), $x = 0.005$ (b), $x = 0.01$ (c), $x = 0.02$ (d), and $\gamma$-irradiated PbS:Bi of $x = 0$ (e), $x = 0.005$ (f), $x = 0.01$ (g), and $x = 0.02$ (h).

(Figure 8). The endothermic peak around 734 °C is attributed to the melting of the nanoparticles. The weight loss between 6 and 21% shows the exceptional stability of the catalyst at high temperature.



https://doi.org/10.1021/acsomega.3c02855
ACS Omega 2023, 8, 47427−47439

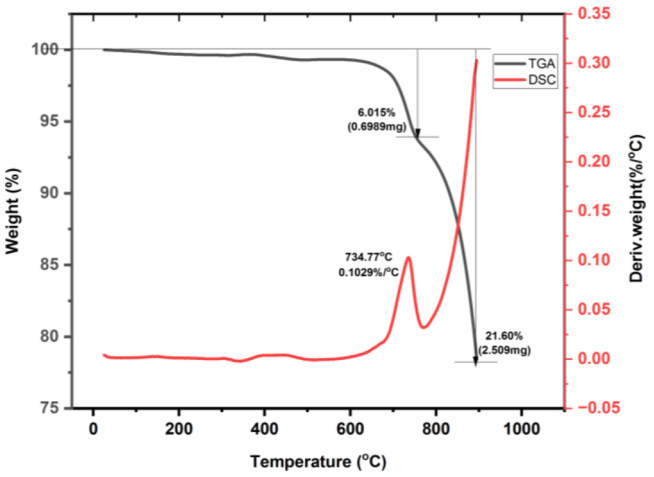


**Figure 8.** TGA-DSC curve for $\gamma$-irradiated $Pb_{0.995}Bi_{0.005}S$.

BET surface area analysis of the irradiated $Pb_{0.995}Bi_{0.005}S$ was performed employing nitrogen adsorption−desorption at 77.35 K, and its corresponding isotherm and multipoint fit are shown in Figure 9. As observed from BET studies, the irradiated $Pb_{0.995}Bi_{0.005}S$ sample has a surface area of 9.350 $m^2$/g. Furthermore, the isotherm of the sample shows type II adsorption with type H3 hysteresis, which is associated with the plate-like layered structure. The distribution of pore volume and pore diameter are 0.028 cc/g and 3.917 nm (Figure 9). Since the irradiated $Pb_{0.995}Bi_{0.005}S$ sample has numerous pores distributed through a wide pore range, this will enhance the number of active sites and boost the photocatalytic activity.

The photocatalytic analysis of both pristine and $\gamma$-irradiated Bi ion-doped PbS was investigated by degrading the MB dye. Initially, MB photolysis was executed by exposing the sample to sunlight for 160 min. Samples were taken at regular intervals of time, and their absorbance was calculated. For photocatalytic dye degradation, the PbS catalyst was loaded with 10 ppm of MB solution having pH 7. After reaching adsorption−desorption equilibrium, the solution was irradiated to sunlight for 160 min. The sunlight-exposed samples were taken at regular intervals, and their absorbance spectra were determined. The MB elevated peak was observed at 663 nm, and it is attributed to its monomer and this peak position remains the same during the entire degradation process. Figure 10 shows $A/A_0$ vs time for pure and $\gamma$-irradiated PbS:Bi and Figure 11 shows $-\ln(A/A_0)$ vs time for pure and $\gamma$-irradiated PbS:Bi.

The percentage of photolysis is very small (12%), so we can conclude that the dye is stable under sunlight. Dye solution degradation efficiency was increased with addition of the catalyst. For pure PbS:Bi catalysts, the degradation efficiencies were 64.37, 62.40, 65.77, and 63.81%, while those of irradiated samples show efficiencies of 66.52, 74.72, 68.14, and 70.85%. Results indicate a remarkable improvement in photocatalytic activity for doped samples after $\gamma$-irradiation. This is due to the sulfur vacancies that are created, which act like trap states and restrict photogenerated electrons and holes from recombination, increasing the degradation rate of organic MB.[60] The highest degradation rate was observed for the $\gamma$-irradiated $Pb_{0.995}Bi_{0.005}S$ photocatalyst, and it was 74.72% at 160 min (Figure 12).

The rate constant of the irradiated $Pb_{0.995}Bi_{0.005}S$ sample was found to be having a maximum value of 0.00798 $min^{-1}$ than other irradiated samples, and this shows enhancement in photocatalytic efficiency (Figure 13). The catalytic stability was checked for gamma-irradiated $Pb_{0.995}Bi_{0.005}S$ in three subsequent cycles by degrading MB, and the decomposition efficiency of the catalyst was analyzed. From the recycling experimental data shown in Figure 14, we understand that there is no photocatalytic loss efficiency in $\gamma$-irradiated $Pb_{0.995}Bi_{0.005}S$ after using it for three cycles.

The main reactive species taking part in the degradation process were investigated by a scavenger test using EDTA as a hole scavenger, $AgNO_3$ as an electron scavenger, and isopropyl alcohol (IPA) as a hydroxyl scavenger radical. During the reaction (Figure 15), the degradation rate of MB is reduced from 74.72 to 21.78% with the addition of EDTA, which suggests that holes are the active species in $\gamma$-irradiated $Pb_{0.995}Bi_{0.005}S$, followed by hydroxyl radicals (IPA), which have a degradation percentage of 43.39%. The same catalyst's reusability was tested, and the catalyst demonstrated excellent stability after three cycles.

The main decomposition mechanism of MB in the investigated PbS:Bi photocatalytic system is as follows. Under high-energy gamma irradiation, PbS:Bi underwent ionization and creates sulfur vacancies with the change in the crystallinity. Since the energy is in the kGy regime, point

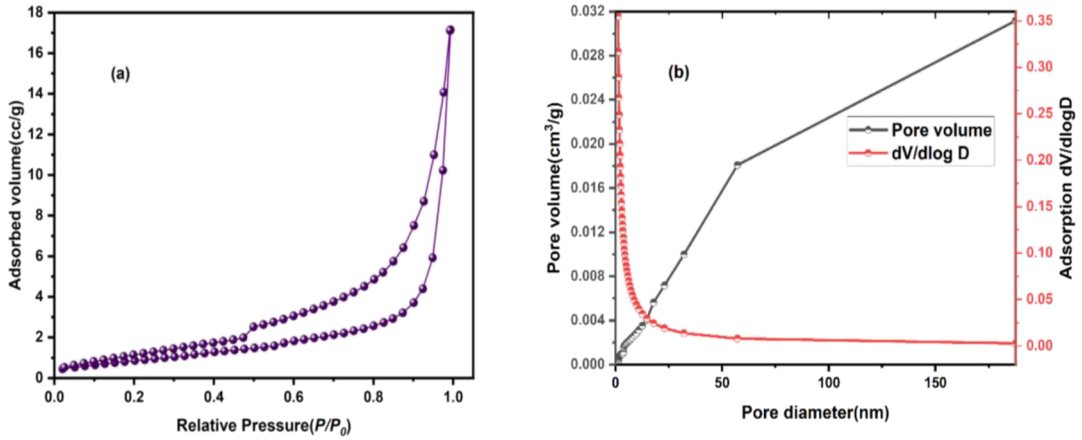


**Figure 9.** (a) Adsorption−desorption isotherm of $\gamma$-irradiated $Pb_{0.995}Bi_{0.005}S$ and (b) plot of BJH adsorption pore volume and d$V$/d log $D$ pore volume against pore diameter for $\gamma$-irradiated $Pb_{0.995}Bi_{0.005}S$.



https://doi.org/10.1021/acsomega.3c02855
ACS Omega 2023, 8, 47427−47439

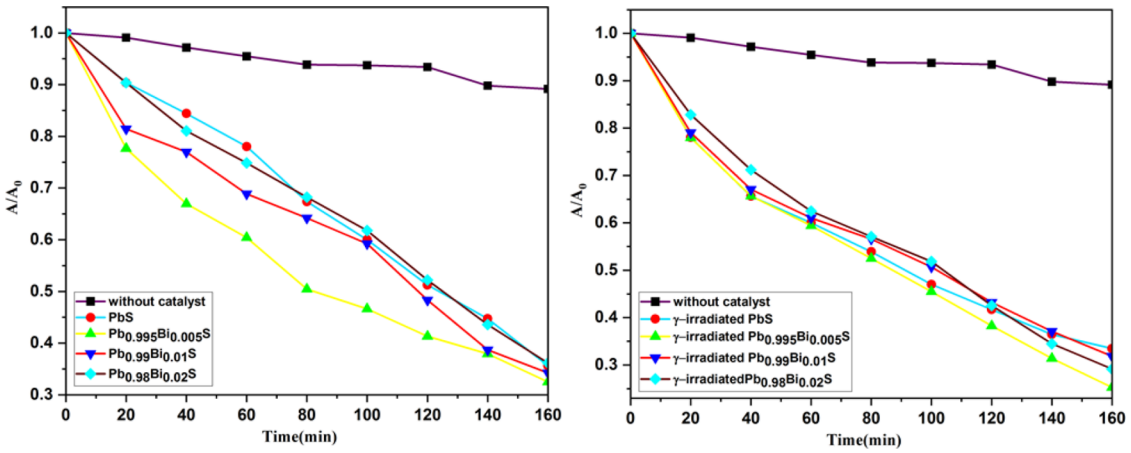


**Figure 10.** $A/A_0$ vs time for pure and $\gamma$-irradiated PbS:Bi.

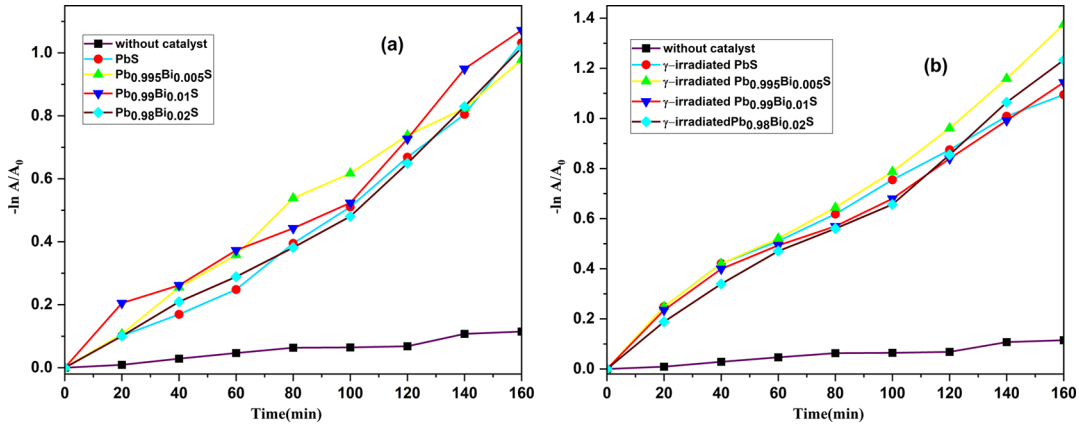


**Figure 11.** $\ln(A/A_0)$ vs time for pure and $\gamma$-irradiated PbS:Bi.

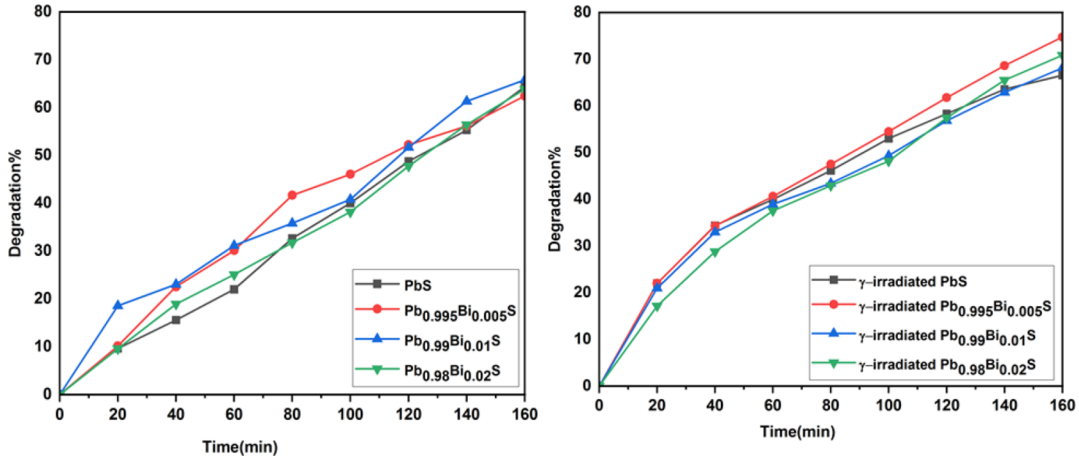


**Figure 12.** Degradation percentage of pure and $\gamma$-irradiated PbS:Bi.

defects and grain boundaries form in PbS. The substitutional heterovalent cationic doping of PbS with Bi ions slows the recombination rate and the lifespan of photoassisted charge carriers is enhanced resulting in improvement of photocatalytic activity.[61] According to the optical studies, the optical bandgap is in the visible range before and after gamma irradiations. Here, the combined effect of $Bi^{3+}$ ions as dopants and the gamma irradiation reduces electron−hole pair recombination in PbS. These photogenerated electron−hole pairs interact with the dye on the PbS catalyst surface. Since oxidizing power of free holes is greater than the reducing power of free electrons, MB adsorbed on the catalyst surface is decomposed by strong reactivity of free holes and hydroxyl radicals derived from them. The process was then repeated until the dye contaminants were completely degraded. Further with ESR we may get better insight into the presence of radicals and the reaction pathway for the photocatalyst.[62,63] Xu et al. conducted spin trapping in conjunction with ESR analysis and examined the free radical responsible for the photocatalytic mechanism.[64]



https://doi.org/10.1021/acsomega.3c02855
ACS Omega 2023, 8, 47427−47439

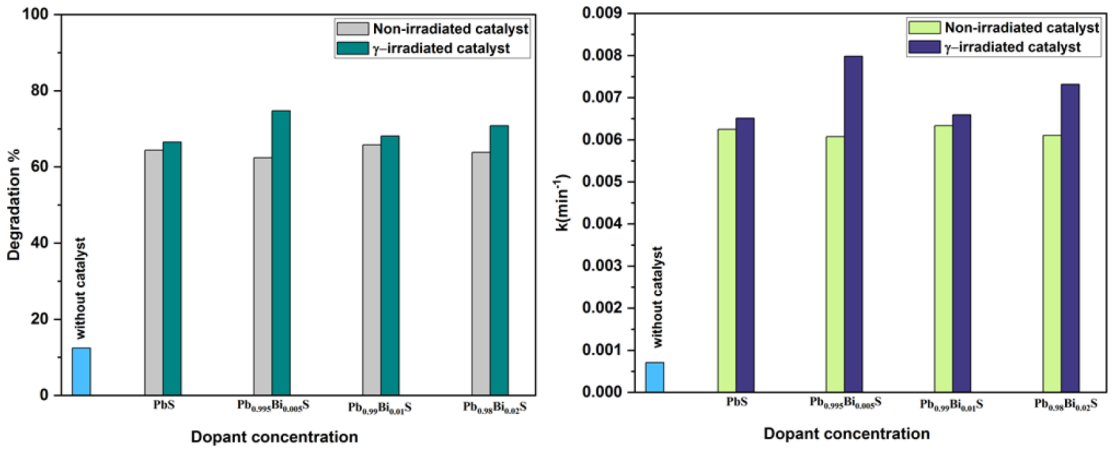


**Figure 13.** Bar chart of degradation and rate constant for pure and $\gamma$-irradiated PbS:Bi.

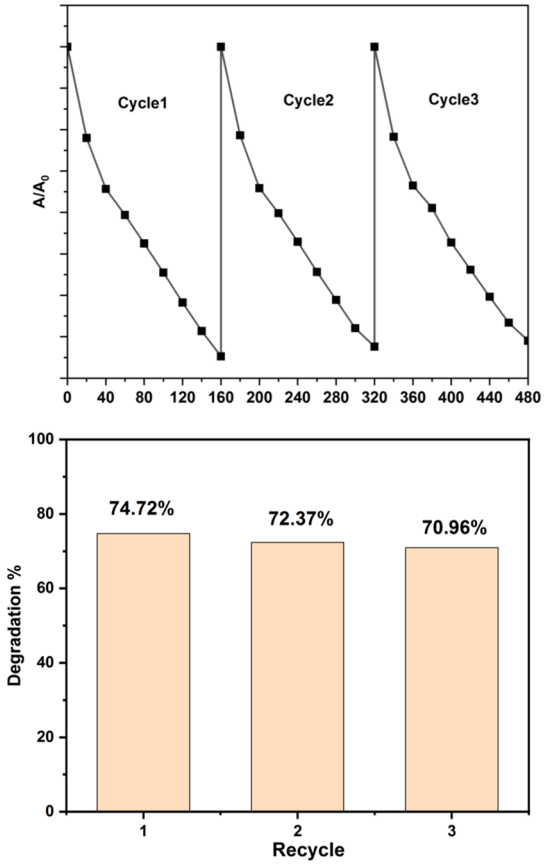


**Figure 14.** Reusability of $\gamma$-irradiated $Pb_{0.995}Bi_{0.005}S$ for MB degradation under sunlight.

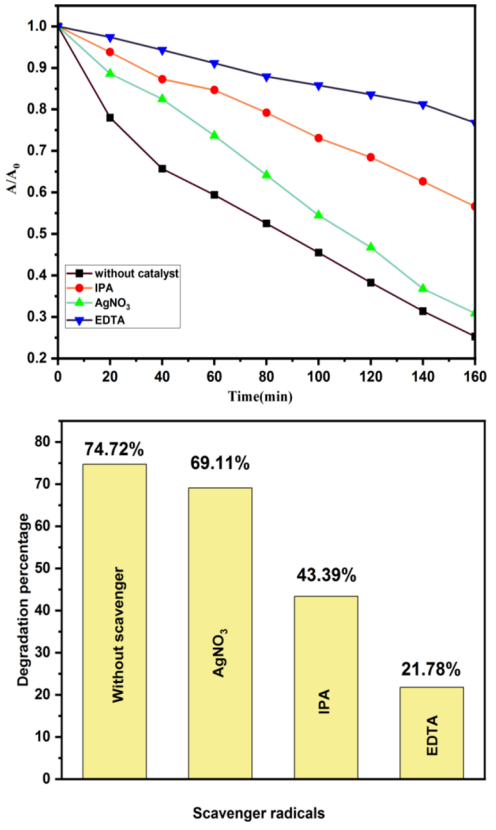


**Figure 15.** Scavenger radical result of $\gamma$-irradiated $Pb_{0.995}Bi_{0.005}S$.

The best catalyst (irradiated $Pb_{0.995}Bi_{0.005}S$) had surface area of 9.350 $m^2/g$ and pore diameter of 3.917 nm, respectively, and was found to have micro and mesoporous distributions. The thermal study of irradiation $Pb_{0.995}Bi_{0.005}S$ revealed that it has an endothermic character and a high degree of thermal stability. The carrier concentration of irradiated $Pb_{0.995}Bi_{0.005}S$, as estimated from room-temperature Hall measurements, is $9.225 \times 10^{15}$ $cm^{-3}$, indicating that the catalyst is a p-type semiconductor. Table 2 compares previously reported PbS for MB dye degradation with our gamma-irradiated PbS:Bi. Numerous investigations on the photocatalytic activity of PbS have been conducted, although the great majority employ ultraviolet light, hence limiting its practical applications.

**Table 2. Comparison of Degradation Efficiency of MB Dye by PbS**

| material | degradation efficiency | light source | time (min) | references |
|---|---|---|---|---|
| PbS | 75.9% | UV light | 180 | 28 |
| Mg and Zn codoped PbS | 80% | UV light | 180 | 29 |
| $PbS/Ni_2P$ | 75% | UV light | 180 | 65 |
| $\gamma$-$Pb_{0.995}Bi_{0.005}S$ | 74.72% | sunlight | 160 | present work |



https://doi.org/10.1021/acsomega.3c02855
ACS Omega 2023, 8, 47427−47439

In our research, gamma irradiation is employed to alter the material characteristics of PbS in order to facilitate MB degradation under visible light. On the basis of obtained values, high-energy gamma irradiation can be employed to alter the photocatalytic property of PbS:Bi for the removal of organic contaminants from industrial effluent under sunlight.

## 4. CONCLUSIONS

Bi ion doped PbS (0, 0.05, 1, 2%) was successfully synthesized employing the co-precipitation technique, and obtained samples were irradiated with high-dosage gamma-rays of 90 kGy. PbS:Bi structural and chemical composition investigation was carried out. According to the optical studies, the optical bandgap is in the visible range. The obtained product's photocatalytic activity was tested to degrade MB dye in visible sunlight. The highest degradation rate was found to be 74.72% for the irradiated $Pb_{0.995}Bi_{0.005}S$ photocatalyst. According to the scavenger test, holes and hydroxyl radicals are active species involved in MB degradation. After three cycles, the best catalyst was found to have a degradation rate of 70.92%. We can conclude from this work that $\gamma$-irradiation can provide a new method for producing efficient photocatalysts for waste water treatment.

## AUTHOR INFORMATION


### Corresponding Authors

**L. Kungumadevi** − *Department of Physics, Mother Teresa Women's University, Kodaikanal 624102, India*; Email: sivarivudevi@gmail.com

**Yuvakkumar Rathinam** − *Department of Physics, Alagappa University, Karaikudi, Tamil Nadu 630003, India*; orcid.org/0000-0001-6779-3453; Email: yuvakkumarr@alagappauniversity.ac.in

### Authors

**Jeya P** − *Department of Physics, CMS College, MG University, Kottayam, Kerala 686560, India; Department of Physics, Mother Teresa Women's University, Kodaikanal 624102, India*

**Keerthana SP** − *Department of Physics, Alagappa University, Karaikudi, Tamil Nadu 630003, India*

**Ravi Ganesan** − *Department of Physics, Alagappa University, Karaikudi, Tamil Nadu 630003, India*

**Asokan Kandasami** − *Materials Science Division, Inter-University Accelerator Centre, New Delhi 110067, India*; Present Address: Department of Physics & Centre for Interdisciplinary Research, University of Petroleum and Energy Studies (UPES) Dehradun, Uttarakhand 248007 India; orcid.org/0000-0002-0613-219X

**T. S. Senthil** − *Department of Physics, Erode Sengunthar Engineering College, Erode 638057, India*; orcid.org/0000-0003-2376-9122

Complete contact information is available at: https://pubs.acs.org/10.1021/acsomega.3c02855


### Notes

The authors declare no competing financial interest.

## ACKNOWLEDGMENTS

The authors sincerely thank IUAC, New Delhi for providing a gamma radiation facility and further help during characterization.

## REFERENCES


(1) Mishra, N.; Vasavi Dutt, V. G.; Arciniegas, M. P. Recent progress on metal chalcogenide semiconductor tetrapod-shaped colloidal nanocrystals and their applications in Optoelectronics. *Chem. Mater.* **2019**, *31*, 9216−9242.

(2) Giuffredi, G.; et al. Transition metal chalcogenides as a versatile and tunable platform for catalytic CO2 and N2 electroreduction. *ACS Mater. Au* **2021**, *1*, 6−36.

(3) Andrade Neto, N. F.; et al. Fast and facile sonochemical synthesis of mg- and Zn-doped PBS nanospheres: Optical properties and photocatalytic activity. *J. Mater. Sci.: Mater. Electron.* **2020**, *31*, 14192−14202.

(4) Zhu, G.; Xu, Z. Controllable growth of semiconductor heterostructures mediated by bifunctional Ag2S nanocrystals as catalyst or source-host. *J. Am. Chem. Soc.* **2011**, *133*, 148−157.

(5) Shi, X.-F.; et al. Multiple exciton generation application of PbS quantum dots in ZnO@PbS/graphene oxide for enhanced photocatalytic activity. *Appl. Catal., B* **2015**, *163*, 123−128.

(6) Jo, I.-R.; et al. Enhanced electrocatalytic activity and electrochemical stability of Cu2S/PbS counter electrode for quantum-dot-sensitized solar cells. *Appl. Surf. Sci.* **2020**, *525*, No. 146643.

(7) Kim, T.; et al. A facet-controlled Rh3Pb2S2 nanocage as an efficient and robust electrocatalyst toward the hydrogen evolution reaction. *Nanoscale* **2018**, *10*, 9845−9850.

(8) Chhabra, V. A.; et al. Pani/PBS QD nanocomposite structure for visible light driven photocatalytic degradation of Rhodamine 6G. *Environ. Res.* **2020**, *186*, No. 109615.

(9) Zhou, M.; et al. Degradation of organics in reverse osmosis concentrate by electro-fenton process. *J. Hazard. Mater.* **2012**, *215*−*216*, 287−293.

(10) Bhuvaneswari, K.; et al. Visible light driven reduced graphene oxide supported znmgal LTH/ZnO/G-C3N4 nanohybrid photocatalyst with notable two-dimension formation for enhanced photocatalytic activity towards organic dye degradation. *Environ. Res.* **2021**, *197*, No. 111079.

(11) Abargues, R.; et al. Enhancing the photocatalytic properties of PbS QD Solids: The ligand exchange approach. *Nanoscale* **2019**, *11*, 1978−1987.

(12) Sathyamoorthy, R.; Kungumadevi, L. Facile synthesis of PbS nanorods induced by concentration difference. *Adv. Powder Technol.* **2015**, *26*, 355−361.

(13) Chen, K.; et al. Enhancing photocatalytic activity of Au-capped CdS−PbS heterooctahedrons by morphology control. *J. Phys. Chem. C* **2020**, *124*, 7938−7945.

(14) Suganya, M.; et al. Enhanced photocatalytic and antifungal properties of Sr-doped PbS nanopowders. *Mater. Technol.* **2018**, *33*, 214−219.

(15) Suganya, M.; et al. Photoconductive, photocatalytic and antifungal properties of PbS:Mo nanoparticles synthesized via precipitation method. *Surf. Interfaces* **2018**, *13*, 148−156.

(16) Liu, L.; et al. Photocatalytic activity of PbS quantum dots sensitized flower-like Bi 2 Wo 6 for degradation of rhodamine B under Visible light irradiation. *J. Mol. Catal. A: Chem.* **2014**, *394*, 309−315.

(17) Wang, T.; et al. Biomass derived the V-doped carbon/Bi2O3 composite for efficient photocatalysts. *Environ. Res.* **2020**, *182*, No. 108998.

(18) Nefzi, C.; et al. Improvement of structural, optical and electrical properties of iron doped indium oxide thin films by high gamma radiations for photocatalysis applications. *Mater. Sci. Semicond. Process.* **2019**, *90*, 32−40.

(19) He, Z.; et al. Construction of cu7s4@cuco2O4 yolk−shell microspheres composite and elucidation of its enhanced photocatalytic activity, mechanism, and pathway for carbamazepine degradation. *Small* **2023**, *19*, No. e2207370.

(20) Dong, D.; et al. Preparation of tio2 photocatalyst microspheres by geopolymer technology for the degradation of tetracycline. *J. Cleaner Prod.* **2022**, *339*, No. 130734.




https://doi.org/10.1021/acsomega.3c02855
*ACS Omega* 2023, 8, 47427−47439

(21) Xiang, X.; et al. Photocatalytic degradation of sulfadiazine in suspensions of TiO2 nanosheets with exposed (001) facets. *Chin. Chem. Lett.* **2021**, *32*, 3215−3220.
(22) He, Z.; Fareed, H.; et al. Mechanistic insight into the charge carrier separation and molecular oxygen activation of manganese doping BiOBr hollow microspheres. *J. Colloid Interface Sci.* **2023**, *629*, 355−367.
(23) Sagadevan, S.; et al. A chemical synthesized Al-doped PbS nanoparticles hybrid composite for optical and electrical response. *J. Mater. Sci.: Mater. Electron.* **2017**, *28*, 10902−10908.
(24) Ahmed, A. M.; Rabia, M.; Shaban, M. The structure and photoelectrochemical activity of Cr-doped PbS thin films grown by Chemical Bath Deposition. *RSC Adv.* **2020**, *10*, 14458−14470.
(25) Rajathi, S.; Kirubavathi, K.; Selvaraju, K. Preparation of nanocrystalline Cd-doped PBS thin films and their structural and optical properties. *J. Taibah Univ. Sci.* **2017**, *11*, 1296−1305.
(26) Ekinci, A.; Şahin, Ö.; Horoz, S. Chemical Bath deposition of Co-doped PBS thin films for Solar Cell Application. *J. Mater. Sci.: Mater. Electron.* **2020**, *31*, 1210−1215.
(27) Kumar, K. N. C.; et al. Influence of nickel on the structural, optical and magnetic properties of PbS thin films synthesized by successive ionic layer adsorption and reaction (SILAR) method. *Mater. Lett.* **2016**, *164*, 108−110.
(28) Rosario, S. R.; et al. Analysis of Cu doping concentration on PBS thin films for the fabrication of solar cell using feasible nebulizer spray pyrolysis. *Mater. Rese. Exp.* **2019**, *6*, No. 056201.
(29) Papagiorgis, P.; et al. The influence of doping on the optoelectronic properties of PbS colloidal quantum dot solids. *Sci. Rep.* **2016**, *6*, 18735.
(30) Koao, L. F.; Hone, F. G.; Dejene, F. B. Synthesis and characterization of PbS nanowires doped with Tb3+ ions by using chemical bath deposition method. *J. Nanostruct. Chem.* **2020**, *10*, 1−7.
(31) Mostovshchikova, E. V.; et al. Lead sulfide films with low iron doping: Correlation between iron position and Optical Properties Evolution. *J. Alloys Compd.* **2021**, *852*, No. 156932.
(32) Ajibade, P. A.; Mbuyazi, T. B.; Oluwalana, A. E. Lead sulphide nanoparticles as photocatalyst for the degradation of methylene blue: Effects of pH, time, adsorption kinetics and recyclability studies. *J. Inorg. Organomet. Polym. Mater.* **2021**, *31*, 2197−2208.
(33) Dong, F.; et al. A semimetal bismuth element as a direct plasmonic photocatalyst. *Chem. Commun.* **2014**, *50*, 10386−10389.
(34) Abhirami, K. M.; Sathyamoorthy, R.; Asokan, K. Structural, optical and electrical properties of gamma irradiated SnO thin films. *Radiat. Phys. Chem.* **2013**, *91*, 35−39.
(35) Mohamed, A. E.-N. A.; et al. Speed response and performance degradation of high temperature gamma irradiated silicon pin photodiodes. *Adv. Sci. Lett.* **2012**, *5*, 74−80.
(36) Baydogan, N.; Ozdemir, O.; Cimenoglu, H. The improvement in the electrical properties of nanospherical ZnO:Al Thin film exposed to irradiation using a Co-60 radioisotope. *Radiat. Phys. Chem.* **2013**, *89*, 20−27.
(37) Sudha, A.; Maity, T. K.; Sharma, S. L. Effects of gamma irradiations on structural and electrical properties of indium oxide thin films prepared by thermal evaporation. *Mater. Lett.* **2016**, *164*, 372−375.
(38) Ali, S. M.; et al. Influence of gamma irradiation on the properties of PbS thin films. *Radiat. Phys. Chem.* **2020**, *171*, No. 108732.
(39) Gupta, R.; Chauhan, R. P.; Kumar, R. Influence of gamma radiation on the optical, morphological, structural and electrical properties of electrodeposited lead selenide nanowires. *Opt. Mater.* **2020**, *99*, No. 109538.
(40) Zhao, C.; et al. Γ-ray induced formation of oxygen vacancies and Ti3+ defects in anatase Tio2 for efficient photocatalytic organic pollutant degradation. *Sci. Total Environ.* **2020**, *747*, No. 141533.
(41) He, Z.; et al. Novel Z-scheme IN2S3/BI2WO6 core-shell heterojunctions with synergistic enhanced photocatalytic degradation of tetracycline hydrochloride. *J. Cleaner Prod.* **2022**, *339*, No. 130634.
(42) Zhang, L.; et al. Recent advances on bismuth-based photocatalysts: Strategies and mechanisms. *Chem. Eng. J.* **2021**, *419*, No. 129484.
(43) Li, Y.; et al. Enhanced visible-light photo-oxidation of nitric oxide using bismuth-coupled graphitic carbon nitride composite heterostructures. *Chin. J. Catal.* **2017**, *38*, 321−329.
(44) Houas, A. Photocatalytic degradation pathway of methylene blue in water. *Appl. Catal., B* **2001**, *31*, 145−157.
(45) International Organization for Standardization. *Fine Ceramics (Advanced Ceramics, Advanced Technical Ceramics)—Determination of Photocatalytic Activity of Surfaces in an Aqueous Medium by Degradation of Methylene Blue*; International Standard Organization: Geneva, Switzerland, 2010.
(46) Yu, J.; et al. Effects of hydrothermal temperature and time on the photocatalytic activity and microstructures of bimodal mesoporous $TiO_2$ powders. *Appl. Catal., B* **2007**, *69*, 171−180.
(47) Cullity, B. D.; Stock, S. R. *Elements of X-Ray Diffraction*, 3rd edition; Prentice-Hall: New Jersey, 2001; pp 167−171.
(48) Jothibas, M.; et al. Synthesis and enhanced photocatalytic property of Ni doped zns nanoparticles. *Sol. Energy* **2018**, *159*, 434−443.
(49) Hastuti, E.; et al. The effects of Fe-doping on MnO2: Phase transitions, defect structures and its influence on electrical properties. *RSC Adv.* **2021**, *11*, 7808−7823.
(50) Peng, S.; et al. Remarkable enhancement of photocatalytic hydrogen evolution over CD 0.5 zn 0.5 s by bismuth-doping. *Int. J. Hydrogen Energy* **2012**, *37*, 1366−1374.
(51) Cao, H.; et al. Growth and photoluminescence properties of PbS nanocubes. *Nanotechnology* **2006**, *17*, 3280−3287.
(52) Krauss, T. D.; Wise, F. W. Raman-scattering study of exciton-phonon coupling in PbS nanocrystals. *Phys. Rev. B* **1997**, *55*, 9860−9865.
(53) Smith, G. D.; et al. First- and second-order Raman spectra of Galena (PbS). *J. Appl. Phys.* **2002**, *92*, 4375−4380.
(54) Kubelka, P.; Munk, F. A contribution to the optics of pigments. *Z. Tech. Phys.* **1931**, *12*, 593−599.
(55) Urbach, F. The long-wavelength edge of photographic sensitivity and of the electronic absorption of Solids. *Phys. Rev.* **1953**, *92*, 1324−1324.
(56) Sarker, P.; et al. Effect of gamma irradiation on structural, morphological and optical properties of thermal spray pyrolysis deposited CuO thin film. *Ceram. Int.* **2021**, *47*, 3626−3633.
(57) Shkir, M.; et al. A facile synthesis of Bi@PbS nanosheets and their key physical properties analysis for Optoelectronic Technology. *Mater. Sci. Semicond. Process.* **2020**, *107*, No. 104807.
(58) Vigil, O.; et al. Characterization of defect levels in chemically deposited CdS films in the cubic-to-hexagonal phase transition. *J. Vac. Sci. Technol., A: Vac., Surf., Films* **1997**, *15*, 2282−2286.
(59) Lee, S. J.; et al. Plasmonic Zno/au/G-C3N4 nanocomposites as solar light active photocatalysts for degradation of organic contaminants in wastewater. *Chemosphere* **2021**, *263*, No. 128262.
(60) Bhardwaj, J.; et al. Gamma irradiation induced surface plasmon resonance of Cu nanoparticles in Fullerene C60. *Surf. Interface Anal.* **2022**, *54*, 1130−1141.
(61) Stavrinadis, A.; et al. Heterovalent cation substitutional doping for quantum dot homojunction solar cells. *Nat. Commun.* **2013**, *4*, 2981.
(62) Xue, S.; et al. Direct Z-scheme charge transfer in heterostructured moo3/G-C3N4 photocatalysts and the generation of active radicals in photocatalytic dye degradations. *Environ. Pollut.* **2019**, *250*, 338−345.
(63) Ding, X.; et al. Self doping promoted photocatalytic removal of no under visible light with BI2MOO6: Indispensable role of superoxide ions. *Appl. Catal., B* **2016**, *182*, 316−325.
(64) Xu, X.; et al. Mechanisms for •O2- and •oh production on flowerlike bivo4 photocatalysis based on Electron Spin Resonance. *Front. Chem.* **2018**, *6*, 64.


https://doi.org/10.1021/acsomega.3c02855
*ACS Omega* 2023, 8, 47427−47439

(65) Liu, S.; Han, L.; Liu, H. Synthesis, characterization and photocatalytic performance of PBS/ni2p flowers. *Appl. Surf. Sci.* **2016**, *387*, 393−398.



https://doi.org/10.1021/acsomega.3c02855
*ACS Omega* 2023, 8, 47427−47439